Volume 17
Number 45
7 December 2021
Pages 10163–10396

Soft Matter

rsc.li/soft-matter-journal

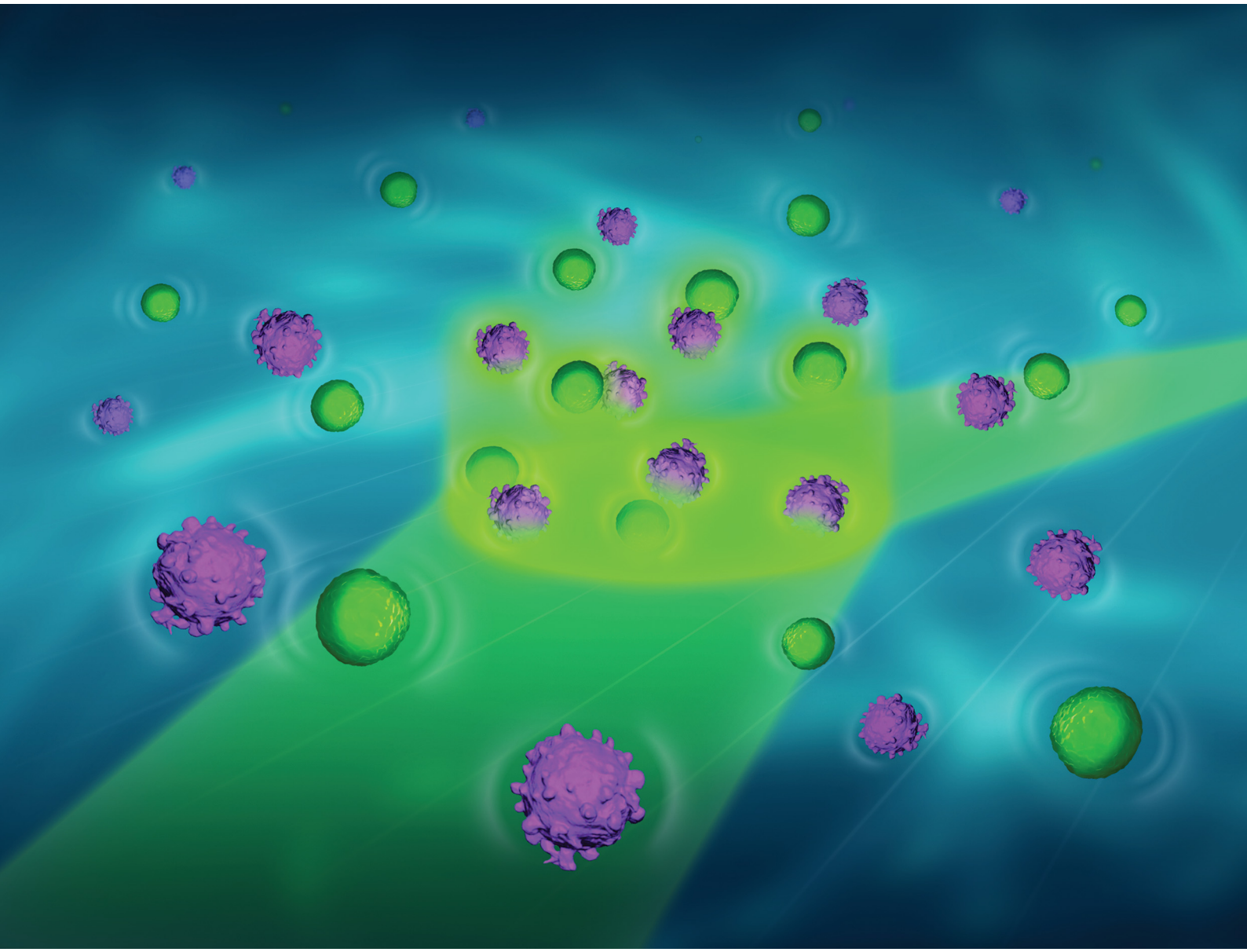

ISSN 1744-6848

ROYAL SOCIETY OF CHEMISTRY

PAPER
Peter R. Lang *et al.*
The effect of morphology and particle–wall interaction on colloidal near-wall dynamics

Soft Matter

PAPER

View Article Online
View Journal | View Issue

Check for updates

Cite this: *Soft Matter*, 2021, **17**, 10301

The effect of morphology and particle–wall interaction on colloidal near-wall dynamics†

J. Alejandro Rivera-Morán, [a] Yi Liu,[a] Samuel Monter, [ab] Chiao-Peng Hsu, ‡[c] Pia Ruckdeschel,[d] Markus Retsch, [d] Maciej Lisicki [e] and Peter R. Lang *[a]

Received 14th August 2021,
Accepted 28th September 2021

DOI: 10.1039/d1sm01191j

rsc.li/soft-matter-journal

We investigated the near-wall Brownian dynamics of different types of colloidal particles with a typical size in the 100 nm range using evanescent wave dynamic light scattering (EWDLS). In detail we studied dilute suspensions of silica spheres and shells with a smooth surface and silica particles with controlled surface roughness. While the near wall dynamics of the particle with a smooth surface differ only slightly from the theoretical prediction for hard sphere colloids, the rough particles diffuse significantly slower. We analysed the experimental data by comparison with model calculations and suggest that the deviating dynamics of the rough particles are not due to increased hydrodynamic interaction with the wall. Rather, the particle roughness significantly changes their DLVO interaction with the wall, which in turn affects their diffusion.

Open Access Article. Published on 29 September 2021. Downloaded on 8/19/2025 10:49:21 AM.
This article is licensed under a Creative Commons Attribution-NonCommercial 3.0 Unported Licence.

1 Introduction

The low Reynolds-number dynamics of particles near a flat interface is generally slower than in bulk and directionally anisotropic due to an increased flow resistance caused by hydrodynamic interaction between particles and the interface. The first theoretical investigations of this effect date back to the early twentieth century,[1,2] while the first experimental verifications[3] only became available in the 1980s. With the modern microscopy and evanescent wave scattering methods[4] that are now available, there have been numerous investigations of colloidal dynamics in the ultimate vicinity of glass surfaces during the last three decades.[5–20] With a few exceptions,[7,8,18] in most of these investigations, data-analysis and interpretation is based on the assumption of particles with smooth surfaces and no static interaction with the wall other than excluded volume. Similarly, in most studies concerning static particle–particle or particle–wall interactions, flat and homogeneous surfaces are assumed.[21–24] Only since synthesis methods have been available, which allow the batch production of particles with controlled surface roughness,[25–27] have systematic studies on the effect of particle roughness become possible.

The rheological behaviour and particle deposition on various kinds of surfaces have been intensively investigated. It was found that in suspensions of rough particles the onset of discontinuous shear thickening is shifted towards lower volume fractions and critical stresses as compared to particles with smooth surfaces.[26,28,29] This effect is commonly attributed to additional tangential stresses caused by hydrodynamic interaction or solid contacts of asperities. The deviation between experientially observed particle deposition rates and values predicted assuming DLVO interaction between bodies with smooth surfaces has been attributed to the neglect of roughness for a long time. Analytical expressions for the interaction potential between rough particles are not available, but simulations suggest that the stabilization barrier of DLVO potentials is significantly reduced by surface roughness.[30,31] An analytical approximation for the interaction energy between a rough particle and a flat surface was given by Suresh *et al.*[32] and verified by total internal reflection microscopy experiments.[33] Jin *et al.*[34] provided the first numerical model for particle deposition including the impact of surface roughness, merging modified expressions for DLVO interactions between rough surfaces and hydrodynamic interaction.

So-called hairy colloids, *i.e.* core–shell particles consisting of a hard particle core carrying polymer brushes, may be regarded as a limiting case of rough particles with extremely pointed asperities and high surface coverage. However, such particles show a qualitatively different rheology, *e.g.*, the presence of the brushes suppresses shear thickening.[35,36] This is attributed to the fact that the brush behaves like a porous shell, reducing the flow resistance as compared to a compact sphere with the same outer radius. The hydrodynamics of such particles can be described by invoking a hydrodynamic penetration length

[a] *Forschungszentrum Jülich, IBI-4, Jülich, Germany. E-mail: p.lang@fz-juelich.de*
[b] *Universität Konstanz, Germany*
[c] *ETH-Zürich, Switzerland*
[d] *Universität Bayreuth, Germany*
[e] *University of Warsaw, Poland*

† Electronic supplementary information (ESI) available. See DOI: 10.1039/d1sm01191j

‡ Present address: Technische Universität München, Germany.

Open Access Article. Published on 29 September 2021. Downloaded on 8/19/2025 10:49:21 AM.
This article is licensed under a Creative Commons Attribution-NonCommercial 3.0 Unported Licence.

which reduces the effective hydrodynamic radius to a value smaller than the outer radius of the core shell particle.[37–39] The same concept can be generally applied to flows past rough surfaces at low Reynolds numbers.[8,40,41] Consequently, rough particles and porous shell particles are expected to show faster near-wall dynamics as compared to smooth particles with the same outer radius.

In our investigation we employed full spherical particles with a smooth surface, micro-porous spherical shells and spherical particles with surface roughness to test this prediction. We used evanescent wave dynamic light scattering (EWDLS) experiments supported by numerical model calculations to study the Brownian particle dynamics parallel to a flat glass wall. After a thorough introduction to the materials and methods in Section 2 and the numerical model in Section 3, we discuss our findings in Section 4.

2 Experimental

2.1 Materials

We investigated three different types of silica particles, namely standard spheres with a smooth surface (SSi), spherical hollow shells (HSi) and spheres with controlled surface roughness (RSi). The HSi particles were synthesized in a three-step procedure consisting of the synthesis of a monodisperse polystyrene latex core by emulsifier-free emulsion polymerisation which was covered by a silica shell applying a Stöber synthesis protocol. After purification and drying the resulting core–shell particles were calcined to burn off the core. The RSi were produced through hetero-aggregation of small particles onto the surface of a large core. Here we used a combination of particles of 150 nm and 8 nm in diameter. In a second step, a smoothing layer was applied to adjust the height of the asperities. The coverage of the RSi was determined by the number ratio of core and asperity particles. The roughness was controlled by adjusting the thickness of the smoothing layer, which also prevents the detachment of asperity particles. Here we applied a 5 nm thick smoothing layer. The synthesis routes to these particles are described in the literature for the HSi[42] and RSi,[25,28] while the SSi are the same as the large particles used in the first step of the two-step procedure leading to the RSi.

All colloids were suspended either in pure (Mili-Q grade) water which has an approximate electrolyte concentration of $c_S \approx 10^{-5}$ mol L^{-1} due to carbon dioxide absorption, corresponding to a Debye screening length of $\lambda_D^{-1} \approx 100$ nm. At larger electrolyte concentrations, all types of particles would aggregate inevitably. To exclude distortions and misinterpretation of evanescent wave DLS data by the formation of aggregates over the experiment duration and their preferred sedimentation, all samples were characterized by bulk DLS before and after the EWDLS experiments. In no case did we find variations of the hydrodynamic radius, beyond experimental error. Prior to DLS and EWDLS measurements, all sample solutions were centrifuged at 800 rpm for about 16 hours to spin down dust and potential aggregates as far as possible.

Table 1 Particle sizes and relative standard deviations determined by different methods. $\langle R_H \rangle$: hydrodynamic radius measured by DLS; $\langle R_G \rangle$, $\langle R \rangle_{SLS}$, $\langle R_C \rangle_{SLS}$: radius of gyration, particle outer radius and core radius determined by SLS; $\langle R \rangle_{TEM}$, $\langle R_C \rangle_{TEM}$: particle outer radius and core radius determined by electron microscopy. All size parameters are given in units of nm and relative standard deviations σ_{SLS}, σ_{TEM} refer to the line above them

Particle type	Smooth, full silica	Hollow silica	Rough silica
Acronym	SSi	HSi	RSi
$\langle R_H \rangle$	77	154	86
$\langle R_G \rangle$	55	(176)	74
$\langle R \rangle_{SLS}$	69	142	—
σ_{SLS}	0.05	0.02	—
$\langle R_C \rangle_{SLS}$	—	128	—
$\langle R \rangle_{TEM}$	65	142	65
σ_{TEM}	0.08	0.03	0.15
$\langle R_C \rangle_{TEM}$	—	132	—

The particle size parameters and their standard deviations measured with different methods are listed in Table 1.

2.2 Methods

2.2.1 Static and dynamic light scattering. Static (SLS) and dynamic (DLS) light-scattering experiments in bulk were performed on a commercial instrument by ALV-Laservertriebsgesellschaft (Langen, Germany), equipped with a 632.8 nm HeNe Laser as the light source, an automated attenuation system, a PerkinElmer avalanche diode and an ALV-6000 correlator. Static scattering intensities $I(Q)$ were obtained over an angular range from 16 to 150 degrees, by measuring diode count rates which were corrected for attenuation, and scattering volume. Experimental particle form factors, $P(Q)$ were determined by normalizing the scattered intensities with the intensity at zero angle which was obtained by extrapolation. Time auto-correlation functions of the scattered intensity $g_2(Q, t)$ were recorded in a range of scattering angles $20^\circ \leq \theta \leq 150^\circ$ in steps of five degrees. Here the scattering vector is $Q = 4\pi n_S \sin(\theta/2)/\lambda_0$ with the solvent refractive index, n_S, and the laser vacuum wavelength λ_0. To determine the particles' Stokes–Einstein diffusion coefficient, D_0, the initial slope of the correlation function $\Gamma = -D_0 Q^2$ was identified by a non-linear least squares fit to a stretched exponential and plotted *vs.* Q^2. The initial slope of this representation is $2D_0$. The particles' hydrodynamic radii, $\langle R_H \rangle$, were calculated *via* the Stokes–Einstein relation, $\langle R_H \rangle = k_B T/6\pi\eta\langle D_0 \rangle$ using $T = 293$ K and $\eta = 1.0$ mPa s for the solvent viscosity, where $k_B T$ is the thermal energy unit. It is understood that for polydisperse samples $\langle R_H \rangle$ is the *z*-average of the radius distribution and $\langle D_0 \rangle$ is the corresponding averaged diffusion coefficient.

2.2.2 Cryo transmission electron microscopy: cryo-TEM. Bright field TEM images were acquired on a ThermoFisher Tecnai Osiris TEM operated at 200 kV. Mean particle radii $\langle R \rangle_{TEM}$ and relative standard deviations σ were determined by averaging over 100 particles at minimum. Since conventional TEM images correspond to two-dimensional (2D) projections of three-dimensional (3D) objects, electron tomography in high angle annular dark field scanning transmission electron microscopy mode was performed to investigate the morphology of the colloidal particles.[43] A series of 2D projections was acquired

 This journal is © The Royal Society of Chemistry 2021

Open Access Article. Published on 29 September 2021. Downloaded on 8/19/2025 10:49:21 AM.
This article is licensed under a Creative Commons Attribution-NonCommercial 3.0 Unported Licence.

while tilting the specimen around an axis perpendicular to the electron beam over the range from −72 to 72 with an increment of 3 degrees. After cross correlation alignment, the 2D images were reconstructed by Expectation Maximization.[44]

2.3 Evanescent wave dynamic light scattering

2.3.1 EWDLS set-up. EWDLS experiments were performed with an instrument built in-house, based on a triple axis diffractometer by Huber Diffraktionstechnik, Rimsting, Germany, which has been described in detail elsewhere.[14] A frequency doubled Nd/Yag Laser (Excelsior; Spectra Physics) with a vacuum wavelength of λ_0 = 532 nm and a nominal power output of 300 mW is used as a light source. The scattering geometry and the definition of the scattering vector and its components parallel and normal to the interface are sketched in Fig. 1. The sample cell (custom-made by Hellma GmbH, Müllheim, Germany) consists of a hemispherical lens as the bottom part, made of SF10 glass, with an index of refraction n_1 = 1.736 at the used wavelength. The lens is covered by a hemispherical dome which contains the colloidal suspension. The incident beam is totally reflected at the flat wall surface of the hemisphere thereby creating an evanescent wave. The evanescent field extends into the particle suspension and is used as the illumination for the dynamic light scattering experiment. The evanescent wave has a wave vector $\mathbf{k}_e$ lying in the intersection of the interface and the plane spanned by incident and reflected beam. The scattering vector $\mathbf{Q} = \mathbf{k}_s - \mathbf{k}_e$, where the wave vector of the scattered light, $\mathbf{k}_s$, can be varied by changing the two angles θ and α_r which define the position of the detecting unit.

The reciprocal penetration depth of the evanescent field is determined by the angle of incidence α_i, the refractive index of the glass n_1 and that of the suspension n_2 as $\kappa/2 = 2\pi\sqrt{(n_1 \sin\alpha_i)^2 - n_2^2}\big/\lambda_0$. The magnitude of the scattering vector component parallel to the interface is given by $Q_\parallel = 2\pi n_2\sqrt{1 + \cos^2\alpha_r - 2\cos\theta\cos\alpha_r}\big/\lambda_0$ while the normal component is $Q_\perp = 2\pi n_2 \sin\alpha_r/\lambda_0$. Here θ is the in-plane and α_r the off-plane angle defining the position of the detector unit with respect to the reflecting interface. The two scattering vector components can be varied independently of each other by changing θ and α_r. To determine the particle dynamics parallel to the interface at a given penetration depth, a series of correlation functions is recorded at a fixed α_r varying $Q_\parallel$ by changing θ. The initial slopes of the correlation functions Γ are determined by converting the experimental curves to field correlation functions, $g_1(t)$, and fitting their short time parts repeatedly with a single exponential starting from a manually chosen number of data points, N_p. When a single fit has converged, N_p is reduced by two and the remaining data are fitted again. With this procedure it is possible to identify a limited range of N_p's where the best fitting values are essentially independent of N_p.[14] The Γ-values from these ranges are plotted *versus* $Q_\parallel{}^2$ to yield a linear slope which according to eqn (6) is the diffusion coefficient parallel to the interface $\langle D_\parallel\rangle(\kappa)$. The latter is a function of the penetration depth, since the experiment integrates over the z-coordinate, normal to the interface, as indicated by the angle brackets. Examples of original correlation functions and data analysis are presented in the ESI.†

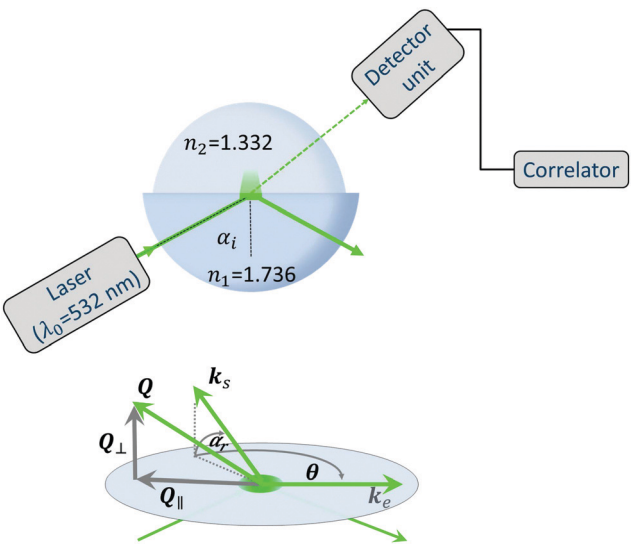

Fig. 1 Sketch of the scattering geometry of an EWDLS experiment with spherical symmetry.

3 Model for numerical calculations

3.1 Near wall dynamics

Suspended particles close to a solid interface show slower Brownian dynamics than in bulk suspension due to hydrodynamic interaction with the wall. Approximations for the resulting friction coefficients in the low Reynolds number limit parallel and normal to the wall were published by Brenner and co-workers.[45,46] Although there are more accurate, but non-analytical expressions *e.g.* ref. 37, we use here the closed approximation to calculate the diffusion coefficient parallel to the wall

$$D_\parallel(z) = D_0\left[1 - \frac{9}{16}\frac{R}{z} + \frac{1}{8}\left(\frac{R}{z}\right)^3 - \frac{45}{256}\left(\frac{R}{z}\right)^4 - \frac{1}{16}\left(\frac{R}{z}\right)^5\right]. \quad (1)$$

For a sphere moving normal to the wall we replaced Brenner's infinite series[46] by the very good closed analytical approximation by Bevan *et al.*[47] to calculate the normal diffusion coefficient.

$$D_\perp(z) = D_0\frac{6z^2 - 10Rz + 4R^2}{6z^2 - 3Rz - R^2}, \quad (2)$$

where z is the shortest distance between the wall and the sphere centre. Since in the EWDLS experiment particles at different distances are illuminated with an exponentially decaying field strength, the experimentally determined diffusion constant is an average over z, weighted with the local field strength. For monodisperse spherical particles that do not experience static interactions with the wall except for excluded volume interactions (hard spheres), the averaged diffusion

Open Access Article. Published on 29 September 2021. Downloaded on 8/19/2025 10:49:21 AM.
This article is licensed under a Creative Commons Attribution-NonCommercial 3.0 Unported Licence.

constants are

$$\langle D_{\parallel,\perp}\rangle(\kappa) = \kappa\int_R^\infty \mathrm{d}z\, D_{\parallel,\perp}(z)\exp\{-\kappa(z-R)\}. \quad (3)$$

If the particles interact with the wall by a static potential $\Phi(z)$ their number density is not independent of z and the average in eqn (3) has to be additionally weighted by the local density, which is written as the Boltzmann factor of the potential *i.e.*

$$\langle D_{\parallel,\perp}\rangle(\kappa) = \frac{\int_R^\infty \mathrm{d}z\exp\{-\beta\Phi(z)\}\exp\{-\kappa z\}D_{\parallel,\perp}(z)}{\int_R^\infty \mathrm{d}z\exp\{-\beta\Phi(z)\}\exp\{-\kappa z\}}, \quad (4)$$

where $\beta = 1/k_BT$ is the reciprocal thermal energy unit. Under the conditions considered so far, the initial slope of the scattered field correlation function can be identified[14] as

$$\Gamma = \frac{\int_R^\infty \mathrm{d}z\exp\{-\beta\Phi(z)\}\exp\{-\kappa z\}\left[D_\parallel(z)Q_\parallel{}^2 + D_\perp(z)\left(Q_\perp{}^2+\kappa^2/4\right)\right]}{\int_R^\infty \mathrm{d}z\exp\{-\beta\Phi(z)\}\exp\{-\kappa z\}} \quad (5)$$

which results in the linear relation

$$\Gamma = \langle D_\parallel\rangle(\kappa)Q_\parallel{}^2 + \langle D_\perp\rangle(\kappa)\left(Q_\perp{}^2+\frac{\kappa^2}{4}\right) \quad (6)$$

with the definitions of diffusion coefficients averaged over the illumination profile given by eqn (4).

3.2 Particle–wall interactions

The interaction potential of the investigated particles with the adjacent glass wall is modelled as a superposition of three contributions,

$$\Phi(z) = \Phi_{\mathrm{vdW}}(z) + \Phi_{\mathrm{er}}(z) + \Phi_{\mathrm{g}}(z) \quad (7)$$

with the van der Waals attraction, $\Phi_{\mathrm{vdW}}(z)$, the electric double layer repulsion, $\Phi_{\mathrm{er}}(z)$, and a gravitational contribution $\Phi_{\mathrm{g}}(z)$ causing particle sedimentation.

The strength of the van der Waals attraction is given by the Hamaker constant, A_{H}, and the dependence on separation distance can be calculated for the sphere wall geometry[48] to yield

$$\Phi_{\mathrm{vdW}}(z) = -\frac{A_{\mathrm{H}}}{6}\left[\frac{R}{z-R}+\frac{R}{z+R}+\ln\left(\frac{z+R}{z-R}\right)\right]. \quad (8)$$

To model the electrostatic repulsion we exploited the linear superposition approach by Lin *et al.*[49]

$$\begin{aligned}\Phi_{\mathrm{er}}(z) &= B_{\mathrm{er}}[(\exp\{-\lambda_{\mathrm{D}}(z-R)\}+\exp\{-\lambda_{\mathrm{D}}(z+R)\})\\ &\quad+(R\lambda_{\mathrm{D}})^{-1}(\exp\{-\lambda_{\mathrm{D}}(z+R)\}-\exp\{-\lambda_{\mathrm{D}}(z-R)\})]\end{aligned} \quad (9)$$

where the amplitude B_{er} is related to the dielectric properties of the medium between the particle and wall and their surface potentials by

$$B_{\mathrm{er}} = 64\pi R\varepsilon\gamma_{\mathrm{p}}\gamma_{\mathrm{w}}\left(\frac{k_BT}{Ze}\right)^2$$

Here, $\varepsilon = \varepsilon_r\varepsilon_0$ where ε_0 is the vacuum permittivity and ε_r is the relative permittivity of the medium, Z is the valency of a single charged site (assumed to be $Z = 1$ in the following), e is the electron unit charge and $\gamma_{\mathrm{p,w}} = \tanh(Ze\Psi_{\mathrm{p,w}}/4k_BT)$ where $\Psi_{\mathrm{p,w}}$ is the surface potential of the particle and the wall, respectively. Since we have no means to assess the surface potential of the wall, we used an effective value $\gamma^2 = \gamma_{\mathrm{p}}\gamma_{\mathrm{w}}$.

The expression of Lin *et al.* is more accurate for the given sphere–wall geometry for all values of λ_DR than the expression which can be derived using Derjaguin's approximation. It is however worthwhile to note that the two expressions differ only by a constant in λ_DR. The ratio of the two expressions is given by $1 - 1/\lambda_DR + (1 + 1/\lambda_DR)\exp\{-2\lambda_DR\}$.

The gravitational contribution to the potential is determined by the buoyancy corrected particle mass

$$\Phi_{\mathrm{g}}(z) = \frac{4\pi}{3}R^3\Delta\rho_{\mathrm{m}}gz \quad (10)$$

where $\Delta\rho_{\mathrm{m}}$ is the particle excess mass density and g is the acceleration of gravity.

For all the calculated data presented in Sections 4.1.2 and 4.2 we replaced the particle radius by the hydrodynamic radius as determined by dynamic light scattering, since for the particles with surface roughness (RSi) a radius cannot be defined meaningfully.

3.3 Particle shape and polydispersity

If the investigated particles have a size distribution, $P(R)$, with a significant width, the expression for the initial slope of the correlation function becomes more complex than eqn (5). In this case the near wall form amplitude $B(Q, R)_{\mathrm{nw}}$ does not cancel from the expression for Γ as in the monodisperse case, and an integration over the size distribution of the numerator and denominator is required to obtain the expression for the size averaged initial slope

$$\langle\Gamma\rangle_{\mathrm{R}} = \frac{\int_0^\infty \mathrm{d}R B_{\mathrm{nw}}{}^2(Q,\kappa,R)P(R)\int_R^\infty \mathrm{d}z\exp\{-\beta\Phi(z)\}\exp\{-\kappa z\}D(Q,\kappa,R)}{\int_0^\infty \mathrm{d}R B_{\mathrm{nw}}{}^2(Q,\kappa,R)P(R)\int_R^\infty \mathrm{d}z\exp\{-\beta\Phi(z)\}\exp\{-\kappa z\}}, \quad (11)$$

where $D(Q, \kappa, R) = D_\parallel Q_\parallel{}^2 + D_\perp(Q_\perp{}^2 + \kappa^2/4)$. For our calculations we used a Gaussian normal distribution with mean value μ and relative standard deviation σ. It is important to note that eqn (11) cannot be strictly reduced to a linear relation similar to eqn (6).

Due to the exponential illumination profile, the form amplitude of a spherical particle cannot be written in a closed analytical form, it is rather given by

$$\begin{aligned}B_{\mathrm{nw}}(Q,\kappa,R) &= 2\pi R^3\left[\int_{-1}^1 \mathrm{d}\mu\int_0^1 \mathrm{d}y\, y^2\cos(Q_\perp y\mu R)\right.\\ &\quad\times\exp\left\{-\frac{y\mu\kappa R}{2}\right\}J_0\left(Q_\parallel\sqrt{1-\mu^2}yR\right)\\ &\quad+i\int_0^1 \mathrm{d}y\, y^2\sin(Q_\perp y\mu R)\\ &\quad\left.\times\exp\left\{-\frac{y\mu\kappa R}{2}\right\}J_0\left(Q_\parallel\sqrt{1-\mu^2}yR\right)\right]\end{aligned} \quad (12)$$

This journal is © The Royal Society of Chemistry 2021

Open Access Article. Published on 29 September 2021. Downloaded on 8/19/2025 10:49:21 AM.
This article is licensed under a Creative Commons Attribution-NonCommercial 3.0 Unported Licence.

where J_0 refers to the zero order Bessel-function of the first kind. For a spherical core–shell particle with a core radius, R_C, outer radius, R, and scattering length densities of the core, ρ_C, and of the shell, ρ_S, the form amplitude is given by

$$B_{nw}(Q_\parallel, Q_\perp, \kappa, R_C, R) = 2\pi R^3 \left(\int_{-1}^{1} d\mu \rho_C \left[\int_0^\chi dy\, y^2 \cos(Q_\perp y\mu R) \exp\left\{ -\frac{y\mu\kappa R}{2} \right\} J_0\left(Q_\parallel \sqrt{1-\mu^2}\, yR \right) + i \int_0^\chi dy\, y^2 \sin(Q_\perp y\mu R) \exp\left\{ -\frac{y\mu\kappa R}{2} \right\} J_0\left(Q_\parallel \sqrt{1-\mu^2}\, yR \right) \right] + \rho_S \left[\int_\chi^1 dy\, y^2 \cos(Q_\perp y\mu R) \exp\left\{ -\frac{y\mu\kappa R}{2} \right\} J_0\left(Q_\parallel \sqrt{1-\mu^2}\, yR \right) + i \int_\chi^1 dy\, y^2 \sin(Q_\perp y\mu R) \exp\left\{ -\frac{y\mu\kappa R}{2} \right\} J_0\left(Q_\parallel \sqrt{1-\mu^2}\, yR \right) \right] \right) \quad (13)$$

where $\chi = R_C/R$. Details of the derivations are given in the ESI.† For the rough particles we could not derive a general expression for the form amplitude. For the limiting case of the particle size being very large compared to the size of the asperities and the asperities being randomly distributed on the particle surface, the form amplitude can be approximated by that of a spherical core particle plus a shell with the scattering length density of the asperities and an effective thickness which is very small compared to the wavelength.

4 Results and discussion

4.1 Experimental findings

4.1.1 Particle characterisation. A thorough characterisation of the used particles was done applying simultaneous static and dynamic light scattering as well as electron microscopy experiments. TEM micrographs and 3D-reconstruction from TEM tomography are shown in Fig. 2 for the RSi and the SSi particles together with TEM and REM images of HSi shells.

From the 3-D reconstructions, it is evident that SSi particles are, although not perfectly, to a good approximation spherical. The RSi particles consist of spherical main bodies carrying asperities on their surface which are irregularly distributed but approximately equal in height. TEM and SEM images from the HSi particles indicate a perfectly spherical shape and a narrow distribution of radii and shell thicknesses. The geometrical parameters and their relative standard deviation are listed in Table 1 together with the results from light scattering measurements. In all cases we observed that the hydrodynamic radius, $\langle R_H \rangle$, is larger than the radius measured in TEM, $\langle R \rangle_{TEM}$. For the rough particles this is intuitively understood, as the TEM radius is that of the central spherical body, which is identical with the SSi radius. The hydrodynamic radius is expected to be larger since the asperities will contribute to the hydrodynamic drag, additionally. In the case of SSi and HSi the discrepancy is explained in part by the fact that the two methods measure different averages of the size distribution. For a Gaussian distribution the ratio of both quantities is related to the relative standard deviation σ by $\langle R_H \rangle / \langle R \rangle_{TEM} = (1 + 3\sigma^2)/(1 + \sigma^2)$, since TEM measures the number average and DLS the z-average of a size distribution. However, for the SSi sample this would account only for about a two percent discrepancy, based on the relative standard deviation observed in TEM. For the HSi sample the expected difference is even smaller. Most likely the discrepancy is explained by the presence of a small fraction of aggregates. In the case of HSi the presence of aggregates with a hydrodynamic radius of $2 \times \langle R \rangle_{TEM}$, the same relative standard deviation as the main population and a relative volume fraction of 5% would account for the deviation.

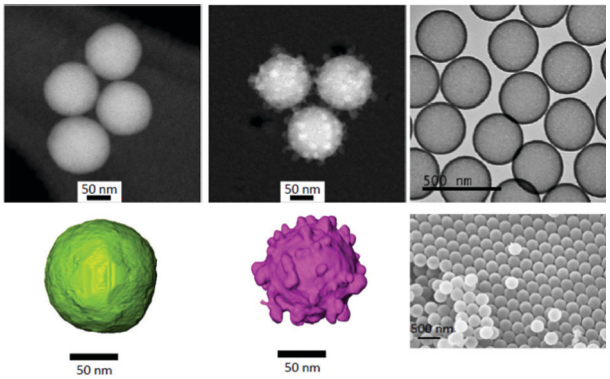

Fig. 2 Micrographs and 3D-reconstructions of SSi (left) and RSI (middle) particles. TEM and REM images of HSi are shown on the right. Scale bars are 50 nm in the left and middle panels and 500 nm in the right column.

The electron microscopy and DLS findings were further underpinned by static light scattering measurements. The radius of gyration, $\langle R_G \rangle$, for the three particle types listed in Table 1 were obtained from Guinier extrapolations. For the HSi particles the ratio $\rho = \langle R_G \rangle / \langle R_H \rangle = 0.71$, which is about ten percent smaller than the expected value for a perfect sphere of $\sqrt{3/5}$. While for the RSi particles we found an intermediate value of $\rho = 0.86$, the value for HSi $\rho = 0.91$, which is about ten percent smaller than expected for an infinitely thin shell. Although these ratios appear reasonable, it has to be noted that the particles sizes (in particular for HSi) are beyond the limits where Guinier's approximation can be safely applied and the values for $\langle R_G \rangle$ should be taken with care. More detailed information can be obtained from the SLS data by analysing the particle form factor. In Fig. 3 we present the experimentally determined $P(Q)$ *vs.* Q data for the SSi and HSi. While the SSi form factor is featureless, the data from the HSi particles show a distinct minimum around $Q \approx 0.022$ nm^{-1}. Non-linear least squares fitting with the form factor for polydisperse spheres and spherical shells[50] resulted in values for radius, shell thickness and relative standard deviations, which are in very good agreement with the TEM data.

4.1.2 EWDLS-data. The experimental findings from evanescent wave DLS are collected in Fig. 4 where we plot the diffusion constants parallel to the interface for the three particle types normalized by their respective bulk diffusion constant as a function of the evanescent wave penetration depth normalized by the bulk hydrodynamic radius.

Open Access Article. Published on 29 September 2021. Downloaded on 8/19/2025 10:49:21 AM.
This article is licensed under a Creative Commons Attribution-NonCommercial 3.0 Unported Licence.

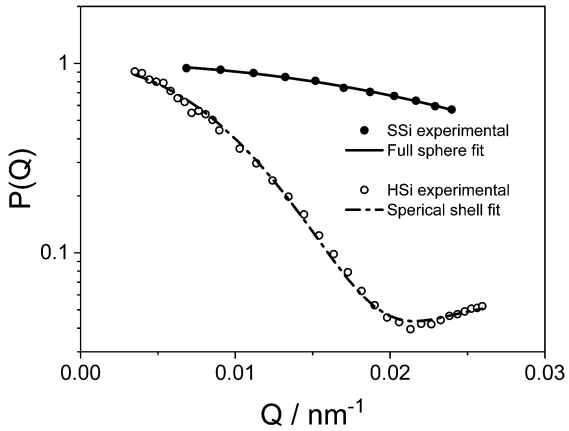

Fig. 3 Particle form factors from static light scattering data of SSi and HSi. Symbols are the experimental data and the lines are non linear least squares fits with the form factor for polydisperse spheres and spherical shells respectively.

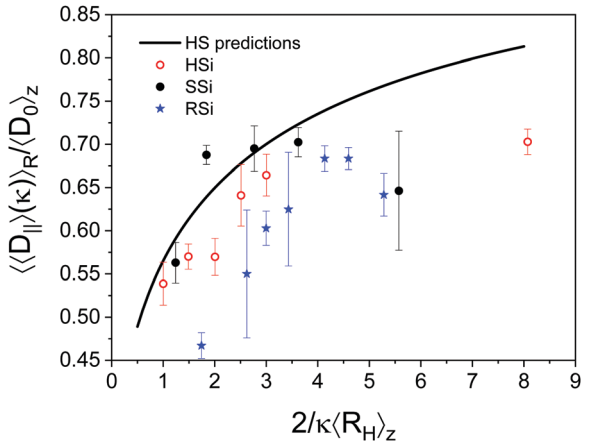

Fig. 4 Normalized parallel diffusion coefficients *versus* normalized penetration depth for three types of particles as indicated in the legend. The symbols are the experimental data and the error bars represent standard deviations from three consecutive experiments. The full line is the prediction for hard sphere particles according to ref. 46.

The data from the SSi particles may be considered to agree, except for one outlier at high penetration depth, with the theoretical reference curve for hard spheres (HS)[46] within experimental scatter. The HSi data are systematically, though not much, smaller than the HS-prediction, while the RSi particles show a significantly slower near wall diffusion than hard sphere particles. While the HSi data follow the trend of the HS-predictions at a somewhat lower level, the RSi data show a qualitatively different behaviour. Except for the outlier at the highest penetration depth, the gradient of the experimental data is always larger than that predicted for the reference system. It is tempting to assign this observation to the particle shape, *i.e.* the surface roughness. However, hydrodynamic theory predicts that surface roughness will reduce the wall drag effect as compared to smooth spherical particles with the same hydrodynamic radius.[37–39]

An alternative interpretation is based on the static interaction between the particles and the glass surface. The theoretical prediction for the near-wall dynamics of hard sphere particles shown in Fig. 4 is based on the assumption that the particle number density, $n(z)$, is constant throughout the entire sample down to the wall. This assumption is invalid, if static interactions other than the excluded volume are effective, as the density depends on the potential by Boltzmann's law. The effect of a DLVO interaction potential plus a gravitational contribution between monodisperse spheres and the wall on $n(z)$ is demonstrated in Fig. 5 for particles with 100 nm radius and fixed Hamaker constant $A_H = 0.5k_BT$. For $B_{er} > A_H$ the near surface region is significantly depleted of particles up to a range of about three particle radii, while an enrichment of particles occurs, if B_{er} is of the order of or smaller than the Hamaker constant. Since the near wall diffusion coefficient increases with separation distance according to eqn (1) it is expected that the experimental values for $\langle D_{\|}\rangle(\kappa)/D_0$ are larger than those predicted for hard spheres, if the static interaction with the wall is mainly repulsive and *vice versa*. We will discuss this effect quantitatively in Section 4.2.

It is worth noting that the gravitational contribution to the interaction potential (*i.e.* sedimentation) causes a shallow (secondary) minimum in the potential, which causes a small (secondary) maximum in the particle density distribution. However, for the particle sizes and density mismatches considered here, the effect of sedimentation on the particle dynamics is negligible as compared to the DLVO interactions.

There are two further effects which might cause the observed deviations of our experimental dynamic data from the hard sphere prediction, *i.e.* particle polydispersity and the resulting influence of the particle form amplitude on the experimental $\langle\Gamma\rangle$-values according to eqn (11) and particle aggregation in combination with enhanced sedimentation of the aggregates. Both effects will also be analysed in detail in Section 4.2.

4.2 Numerical calculations

4.2.1 Polydispersity and form amplitudes. For polydisperse systems the particle form amplitudes do not cancel from the expression for the initial slope of the time correlation function

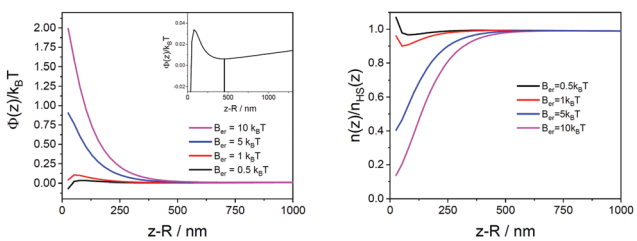

Fig. 5 Left: Sphere-wall interaction potentials calculated with eqn (7) for R = 100 nm, $A_H = 0.5k_BT$, $\lambda_D^{-1} \approx 100$ nm, $\Delta\rho_m = 1$ g mL^{-1} and amplitudes of the electrostatic repulsion B_{er} as indicated in the legend. The inset highlights the shallow minimum, marked by the vertical line for the potential with $B_{er} = 0.5k_BT$ which is due to the gravitational contribution. Right: Particle number densities normalized by the value for hard spheres *versus* separation distance, calculated with Boltzmann's law, using the potentials shown in the left panel.

This journal is © The Royal Society of Chemistry 2021

Open Access Article. Published on 29 September 2021. Downloaded on 8/19/2025 10:49:21 AM.
This article is licensed under a Creative Commons Attribution-NonCommercial 3.0 Unported Licence.

(eqn (11)). If the particles are large enough to cause a strong variation of the scattered field with the scattering angles, significant deviations from the linear $\langle\Gamma\rangle_R$ *vs.* $Q_\parallel{}^2$ relation will occur, as is shown in the inset of Fig. 6, where the subscript R indicates integration over the distribution of particle sizes. This would lead to artefacts, if eqn (6) was applied to determine $\langle D_\parallel\rangle$ (κ) over the full range of scattering vectors. However, for $Q_\parallel R \ll 1$ the linear relation may still be used to determine a mean diffusion coefficient, $\langle\langle D_\parallel\rangle(\kappa)\rangle_R$. Resulting normalized data, calculated using eqn (1), (2), (6), (11) and (13) for a system of hollow shell particles with constant shell thickness and a Gaussian distribution of the outer radius are shown in Fig. 6. The number average outer particle radius, μ, and the shell thickness were chosen to roughly match the HSi particle size determined by TEM. To warrant comparability with the experimental EWDLS data, the calculated data have to be normalized by the z-average of the radius $\langle R\rangle_z$ and the corresponding diffusion coefficient $\langle D_0\rangle_z$, since light scattering experiments measure these quantities.

In all calculations concerning polydisperse or aggregating (Section 4.2.2) systems a density mismatch of $\Delta\rho_m = 1$ g mL^{-1} was incorporated to consider the enhanced sedimentation of larger particles. At low penetration depths systematic deviations from the prediction for monodisperse hard spheres towards slower dynamics are observed. However, the deviation is smaller than typical experimental scatter. Only at the largest polydispersity, and high penetration depths a significant deviation towards faster diffusion coefficients occurs. Similarly small effects are observed for spherical particles, where generally, the effect of polydispersity becomes larger with decreasing particle size, which is shown in the ESI.†

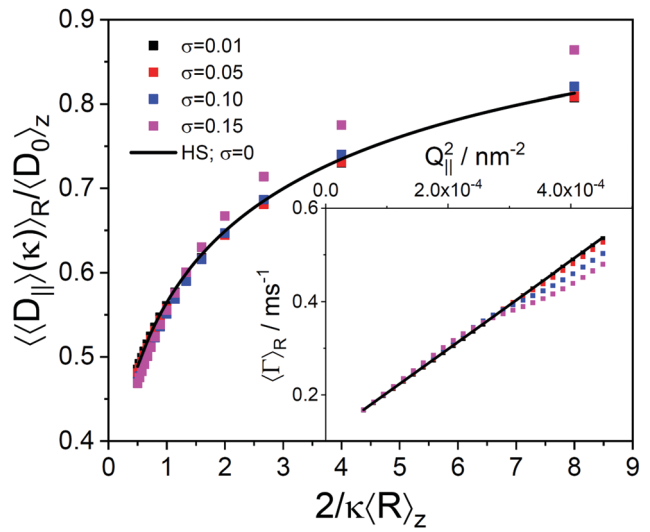

Fig. 6 Normalized parallel diffusion coefficients *versus* normalized penetration depth for hollow shells interacting only by excluded volume, with a constant shell thickness of 20 nm and a Gaussian distribution of the outer radius with μ = 150 nm and relative standard variations as indicated in the legend. Inset: Dependence of the initial relaxation rate on $Q_\parallel{}^2$. Symbols are the data calculated using eqn (1), (2), (6), (11) and (13). The full line is the prediction for monodisperse hard sphere particles according to Brenner.[46]

An analytical expression for $B(Q)$ of rough particles is in general not available. However, assuming that the asperities are small compared to the overall particle size, their average separation distance is small compared to the laser wavelength and they are randomly distributed, the form amplitude can be approximated by that of a spherical core particle plus a thin shell with the scattering length density of the asperities and an effective thickness which is very small compared to the reciprocal scattering vector. We may therefore assume that the effect of form amplitude and polydispersity is similarly small as observed for spheres and spherical shells.

4.2.2 Particle aggregation. As we realized that the three particle types, which we investigated experimentally, had a high tendency to form irreversible aggregates at salt concentrations as low as 0.1 mM, we tested what effect the presence of aggregates and their enhanced sedimentation would have on the near-wall dynamics. To simply mimic the aggregates, we used a bimodal Gaussian size distribution and the form amplitude of spheres to calculate initial slopes with eqn (11). The distribution of the population representing the aggregates is characterized by the mean μ_{agg} which was chosen to be an integer multifold of μ and the relative standard deviation $\sigma_{agg} = \sigma$. Furthermore, the relative volume fraction of the aggregates was varied over a range of $10^{-4} \leq \phi_{agg} \leq 0.05$. Larger volume fractions were not considered, since they would have been detected in the bulk DLS experiments, which were performed after the EWDLS measurements. Similar to the observations on the effect of polydispersity, we found that the linear dependence of $\langle\Gamma\rangle$ on $Q_\parallel{}^2$ is violated by the presence of aggregates, nevertheless it is possible to determine the near wall diffusion coefficient from the linear slope at sufficiently low $Q_\parallel$.

Calculated data of the normalized diffusion coefficients *vs.* normalized penetration depth are shown in Fig. 7 for a system consisting of a major population with μ = 100 nm and minor populations with μ_{agg} varying up to 1000 nm and ϕ_{agg} = 0.05 (left panel). Obviously, the presence of aggregates causes a strong slowing down of the system's near wall dynamics, even if the average hydrodynamic radius of the aggregates is only twice the size of the single particles. Data for this size ratio and varying relative volume fraction of the minor population is shown in the right panel of Fig. 7. The dynamics of the system with $\mu_{agg} = 2\mu$ and $\phi_{agg} \approx 0.03$ shows a similar deviation from the monodisperse reference system as the experimental HSi data. However, in all cases the calculated data show a smaller gradient than the reference systems which is clearly different from the trend of the experimental RSi data.

4.2.3 Static particle–wall interaction. The effect of static particle wall interactions on the near wall dynamics is demonstrated in Fig. 8 for spherical particles and selected interaction potentials. In the left panel, we plot the dynamic data for the interaction potentials shown in Fig. 5. At a typical Hamakaer constant of $A_H = 0.5k_BT$, the dynamics are slower than that of the reference hard sphere system at small penetration depths. At high penetration depths, the calculated data approach the hard sphere data for low electrostatic repulsion and the dynamics become even faster,

Open Access Article. Published on 29 September 2021. Downloaded on 8/19/2025 10:49:21 AM.
This article is licensed under a Creative Commons Attribution-NonCommercial 3.0 Unported Licence.

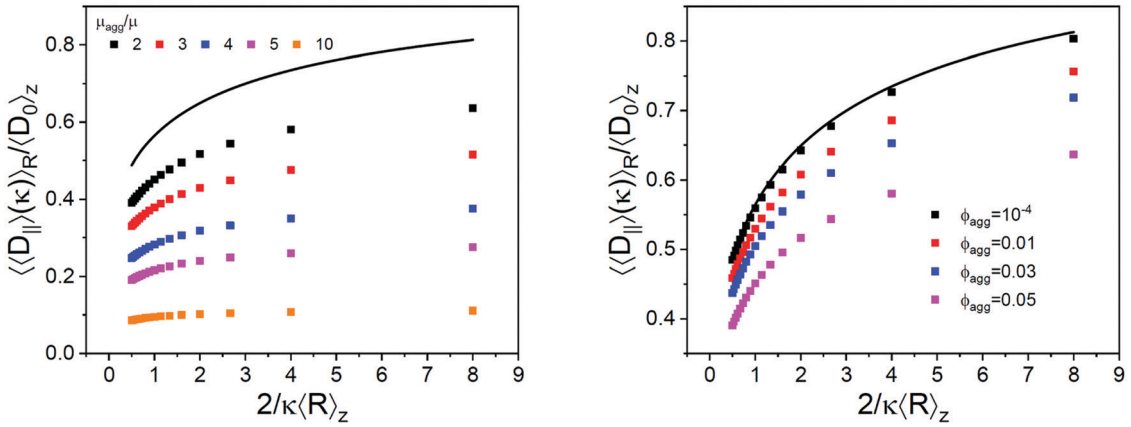

Fig. 7 Normalized parallel diffusion coefficients *versus* normalized penetration depth for systems of spheres with a bimodal Gaussian size distribution. The major population has a number average size of μ = 100 nm and both populations have a relative standard deviation of σ = 0.05. Left panel: The minor population has a relative volume fraction of ϕ_{agg} = 0.05 and their mean size μ_{agg} is varied as indicated in the legend. Right panel: The minor population has a number average size of $\mu_{agg} = 2\mu$ and varying relative volume fractions as indicated in the legend. Symbols are the data calculated using eqn (1), (2), (6), (11) and (12). The full line is the prediction for monodisperse hard sphere particles according to Brenner.[46]

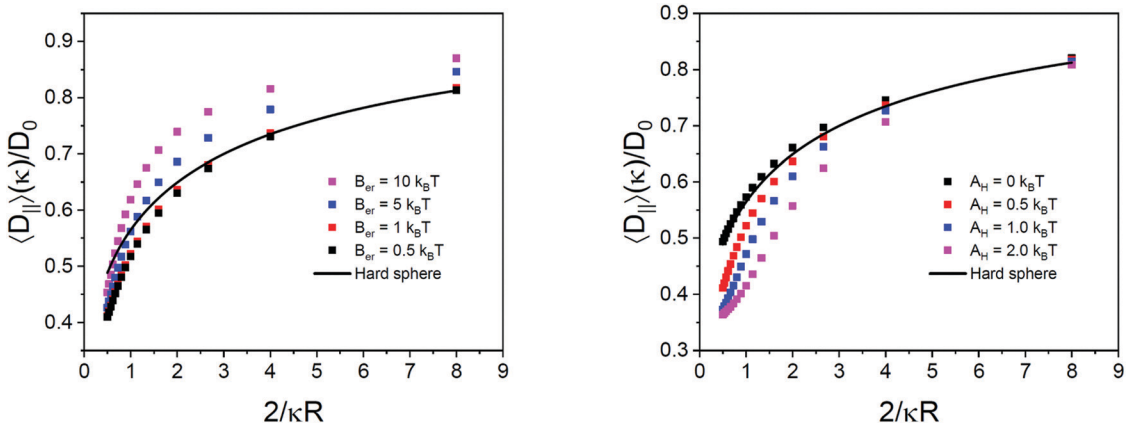

Fig. 8 Normalized parallel near wall diffusion coefficients *versus* normalized penetration depth for spherical particles interacting with the wall by the potentials displayed in Fig. 5 (left) and with $B_{er} = 1k_BT$ (right) and varying Hamaker constants as indicated in the legend. In all cases the excess mass density was chosen $\Delta\rho_m$ = 1 g mL^{-1}. Symbols are data calculated using eqn (1), (2), (6), (11) and (12). The full line represents the prediction for the hard sphere reference system according to Brenner.[46]

if the amplitude of the electrostatic repulsion significantly exceeds the Hamaker constant. The penetration depth at which the crossover of the calculated data with the reference data occurs shifts to smaller penetration depths with increasing electrostatic repulsion.

In the right panel of Fig. 8 we show the influence of varying Hamaker constants at a constant moderate electrostatic repulsion on the near-wall dynamics. At finite Hamaker constants, the calculated values are slower than those of the reference system, for almost all penetration depths. Only at the largest penetration depth investigated, the calculated dynamics appear to converge towards the reference data. At Hamaker constants $A_H \geq B_{er}$ the calculated data deviate from the reference data similarly to the experimental data of the RSi system.

4.2.4 Comparison of experimental EWDLS data with the calculated data. In Fig. 9 we show the experimental EWDLS result from Fig. 4 again, together with sets of calculated dynamic data, which match the measured data within the experimental scatter. The data were calculated with eqn (1), (2), (6), and (11) and the near wall form amplitude of spherical particles. Eqn (12) is a reasonable approximation, since the influence of the form amplitude together with polydispersity is minor as discussed in Section 4.2.1. Additionally we applied a bimodal size distribution to mimic the effect of a small fraction of aggregates, which were assumed to have the double size of the monomeric sphere and the same polydispersity. The parameters used for the calculations are listed in Table 2 and in all cases we applied an excess mass density of $\Delta\rho_m$ = 1 g mL^{-1} and a Debye screening length of λ_D^{-1} = 96 nm. Furthermore, the particles mimicking aggregates were subject to the same interaction potential as the monomers.

For the SSi- and HSi-system we could obtain a reasonable match of calculated with experimental data using an amplitude of the electrostatic repulsion of the order of k_BT and some

 This journal is © The Royal Society of Chemistry 2021

Open Access Article. Published on 29 September 2021. Downloaded on 8/19/2025 10:49:21 AM.
This article is licensed under a Creative Commons Attribution-NonCommercial 3.0 Unported Licence.

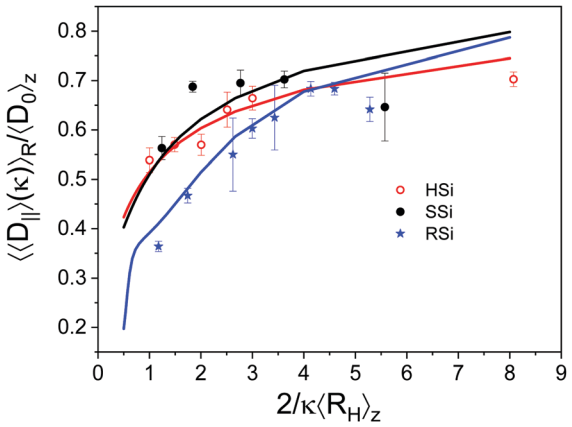

Fig. 9 Normalized parallel diffusion coefficients *versus* normalized penetration depth. Symbols are experimental data from the SSi-, the HSi- and the RSi-system, as indicated in the legend. Full lines represent data calculated using eqn (1), (2), (6), (11) and (12) and the parameters listed in Table 2.

Table 2 System parameters used to calculate the dynamic data shown in Fig. 9

Particle type	$\langle R_H\rangle_z$ (nm)	σ	B_{er} (k_BT)	A_H (k_BT)	ϕ_{agg}
SSi	71	0.05	1.5	0.5	5×10^{-3}
HSi	154	0.05	1.0	0.25	0.03
RSi	80	0.05	1.5	2.75	5×10^{-3}

fraction of k_BT for the Hamaker constant. The electrostatic amplitude of the particle–wall interaction corresponds to an effective surface potential $\Psi_{p,w} \approx -2$ mV which is about an order of magnitude smaller than that reported in the literature[51–53] based on total reflection microscopy measurements of the interaction potential between 2 μm Stöber–Silica particles and fused silica microscopy slides. Similarly, the ζ-potentials of all three systems are in the range of −30 to −40 mV. However it is important to note that the value of B_{er} is determined by the product of the particle's and wall's surface potentials. In the present case, the wall consists of a special high refractive index quartz glass (SF10) and there are indications in the literature that the surface charge density of quartz may[54] be one to two orders of magnitude lower than that of silica.[55] We therefore reckon that the small value of B_{er} is due to the low surface potential of the wall. Finally, the B_{er}-values for all three systems investigated here are about equal, which makes us confident that they are reliable. The found Hamaker constants of order $A_H \leq k_BT$ are in the range expected for non-retarded van der Waals interactions calculated based on the Lifshitz theory[56] for silica interacting with quartz across water.

In the case of the HSi-system, we had to allow for a higher relative volume fraction of "aggregates" to obtain a satisfying match of the calculated data with experiments. This is probably due to the fact that HSi particles were calcined and thus dried during synthesis to remove the organic core onto which the silica shell had been grown.[42] The probability of aggregates, which were not properly dispersed, being present is therefore higher than in samples which were never dried. Furthermore, spinning down aggregates is less effective than with full body particles due to the reduced excess mass density.

The most striking finding is, however, that for the RSi-particles the Hamaker constant required to allow for a match of calculated with experimental data is an order of magnitude larger than for the HSi- and SSi-systems. This implies that surface roughness plays an important role for the particle wall interaction and the resulting near wall dynamics. It is known from simulation work that surface roughness will enhance both electrostatic repulsion and van der Waals attraction, simply because the effective surface to surface separation is reduced by asperities. Walz *et al.* reported a lowering of the stabilisation barrier of the resulting DLVO-potential by about 10 to 15%, due to the different distance dependence of attraction and repulsion.[31] A similar reduction of the stabilization barrier was reported by Bhattacharjee *et al.*[30] Furthermore, these authors observe that the primary minimum of the DLVO interaction potential completely vanishes due to asperities. This might explain why our rough particles do not stick irreversibly to the glass surface, despite the large Hamaker constant. In this respect our findings may be regarded as additional experimental evidence for the predicted roughness effects on DLVO interaction energies. The resulting deviation of the dynamic data from the predictions for the reference hard sphere system are a mere consequence of the particle wall interaction potential and the resulting variation of number density with separation distance over which EWDLS inherently integrates.

Our findings might pave the way to a new method for the measurement of static particle wall interactions. Although the technique, especially the data analysis by comparison to model calculations, is cumbersome and not very efficient at this time, it might provide an extension of the classical total internal reflection microscopy (TIRM) technique.[57] While TIRM requires particle sizes which are typically in the range of several micrometres, EWDLS allows measurements on particles as small as 30 nm in radius.[14]

5 Conclusions

The Brownian near wall dynamics of different types of suspended silica particles were examined by evanescent dynamic light scattering. While the experimental averaged diffusion coefficients parallel to the wall for smooth full spheres (SSi) and hollow spherical porous shells (HSi) might be considered to be in qualitative agreement with theoretical predictions for the hard sphere reference system, particles with a rough surface (RSi) show significant deviations. The averaged diffusion constants are significantly smaller than for smooth non-interacting particles which is in conflict with hydrodynamic theory.[37–39] To interpret these observations, systematic numerical calculations were performed to investigate the effect of particle polydispersity, the presence of aggregates and static particle–wall interactions on the dynamics. By comparison with experimental data we found that

Open Access Article. Published on 29 September 2021. Downloaded on 8/19/2025 10:49:21 AM.
This article is licensed under a Creative Commons Attribution-NonCommercial 3.0 Unported Licence.

for the SSi and HSi systems very good agreement can be obtained by including a small fraction of aggregates and a particle–wall DLVO interaction, with a Hamaker constant and an amplitude of the electric double layer repulsion, both in the range of $\approx k_BT$. For the RSi system, at least a five times higher Hamaker constant needs to be taken into account to match the calculated data to the experimental results. Despite the high Hamaker constant the rough particles do not adsorb to the wall irreversibly. Both findings are consistent with the simulation results, which show that the DLVO stabilization barrier is significantly reduced by surface roughness[31] and that the primary DLVO minimum completely vanishes for rough particles.[30] We conclude that particle near wall dynamics are very sensitive to surface roughness where the theoretically predicted reduction of the flow resistance can be largely overcompensated by the effect of static particle wall interaction and the resulting particle number density profile.

Author contributions

J. Alejandro Rivera-Morán: investigation, formal analysis, writing – review and editing; Yi Liu: investigation, formal analysis, validation, writing – review and editing; Samuel Monter: investigation, formal analysis, software, validation, writing – review and editing; Chiao-Peng Hsu: resources, writing – review and editing; Pia Ruckdeschel: resources; Markus Retsch: resources, writing – review and editing; Maciej Lisicki: funding acquisition, conceptualization, writing – review and editing; Peter R. Lang: conceptualization, funding acquisition, software, supervision, writing – original draft.

Conflicts of interest

There are no conflicts to declare.

Acknowledgements

We thank Sara Bals, Qiongyang Chen and Hans Vanrompay from EMAT at the University of Antwerp for the TEM-investigation of the SSi and RSi particles and we gratefully acknowledge helpful discussions with Jan Dhont, Gerhard Nägele and Gunwoo Park from Forschungszentrum Jülich GmbH, IBI-4. This work has received funding from the European Union's Horizon 2020 research and innovation programme under grant agreement No 731019 (EUSMI).

Notes and references

1 H. A. Lorentz, *Abhandlung über Theoretische Physik: Ein allgemeiner Satz, die Bewegung einer reibenden Flüssigkeit betreffend, nebst einigen Anwendungen desselben*, B.G. Teubner, Leipzig and Berlin, 1907.
2 H. Faxén, *Ark. Mat. Astron. Fys.*, 1923, **17**, 1.
3 Z. Adamczyk, M. Adamczyk and T. van de Ven, *J. Colloid Interface Sci.*, 1983, **96**, 204–213.
4 K. H. Lan, N. Ostrowsky and D. Sornette, *Phys. Rev. Lett.*, 1986, **57**, 17–20.
5 B. Lin, J. Yu and S. A. Rice, *Colloids Surf., A*, 2000, **174**, 121–131.
6 B. H. Lin, J. Yu and S. A. Rice, *Phys. Rev. E: Stat. Phys., Plasmas, Fluids, Relat. Interdiscip. Top.*, 2000, **62**, 3909–3919.
7 H. B. Eral, F. Mugele and M. H. G. Duits, *Langmuir*, 2011, **27**, 12297–12303.
8 J. Y. Walz and L. Suresh, *J. Chem. Phys.*, 1995, **103**, 10714–10725.
9 L. Joly, C. Ybert and L. Bocquet, *Phys. Rev. Lett.*, 2006, **96**, 046101.
10 M. Hosoda, K. Sakai and K. Takagi, *Phys. Rev. E: Stat. Phys., Plasmas, Fluids, Relat. Interdiscip. Top.*, 1998, **58**, 6275–6280.
11 M. I. Feitosa and O. N. Mesquita, *Phys. Rev. A: At., Mol., Opt. Phys.*, 1991, **44**, 6677–6685.
12 N. Garnier and N. Ostrowsky, *J. Phys. II*, 1991, **1**, 1221–1232.
13 P. Holmqvist, J. K. G. Dhont and P. R. Lang, *Phys. Rev. E: Stat., Nonlinear, Soft Matter Phys.*, 2006, **74**, 021402.
14 P. Holmqvist, J. K. G. Dhont and P. R. Lang, *J. Chem. Phys.*, 2007, **126**, 044707.
15 M. Lisicki, B. Cichocki, J. K. G. Dhont and P. R. Lang, *J. Chem. Phys.*, 2012, **136**, 204704.
16 M. Lisicki, B. Cichocki, S. A. Rogers, J. K. G. Dhont and P. R. Lang, *Soft Matter*, 2014, **10**, 4312–4323.
17 Y. Liu, J. Blawzdziewicz, B. Cichocki, J. K. G. Dhont, M. Lisicki, E. Wajnryb, Y.-N. Young and P. R. Lang, *Soft Matter*, 2015, **11**, 7316–7327.
18 Y. Liu, N. Claes, B. Trepka, S. Bals and P. R. Lang, *Soft Matter*, 2016, **12**, 8485–8494.
19 V. N. Michailidou, G. Petekidis, J. W. Swan and J. F. Brady, *Phys. Rev. Lett.*, 2009, **102**, 068302.
20 V. N. Michailidou, J. W. Swan, J. F. Brady and G. Petekidis, *J. Chem. Phys.*, 2013, **139**, 164905.
21 D. Grasso, K. Subramaniam, M. Butkus, K. Strevett and J. Bergendahl, *Rev. Environ. Sci. Biotechnol.*, 2002, **1**, 17–38.
22 D. Kleshchanok, R. Tuinier and P. R. Lang, *Smart Colloidal Mater.*, 2008, **20**, 073101.
23 Q. Li, U. Jonas, X. S. Zhao and M. Kappl, *Asia-Pac. J. Chem. Eng.*, 2008, **3**, 255–268.
24 V. Dahirel and M. Jardat, *Curr. Opin. Colloid Interface Sci.*, 2010, **15**, 2–7.
25 M. Zanini, C.-P. Hsu, T. Magrini, E. Marini and L. Isa, *Colloids Surf., A*, 2017, **532**, 116–124.
26 L. C. Hsiao, S. Jamali, E. Glynos, P. F. Green, R. G. Larson and M. J. Solomon, *Phys. Rev. Lett.*, 2017, **119**, 158001.
27 L. C. Hsiao and S. Pradeep, *Curr. Opin. Colloid Interface Sci.*, 2019, **43**, 94–112.
28 C.-P. Hsu, S. N. Ramakrishna, M. Zanini, N. D. Spencer and L. Isa, *Proc. Natl. Acad. Sci. U. S. A.*, 2018, **115**, 5117–5122.
29 D. Lootens, H. van Damme, Y. Hémar and P. Hébraud, *Phys. Rev. Lett.*, 2005, **95**, 268302.
30 S. Bhattacharjee, C.-H. Ko and M. Elimelech, *Langmuir*, 1998, **14**, 3365–3375.
31 J. Y. Walz, *Part. Surf.*, 2002, **7**, 151–169.

 This journal is © The Royal Society of Chemistry 2021

Open Access Article. Published on 29 September 2021. Downloaded on 8/19/2025 10:49:21 AM.
This article is licensed under a Creative Commons Attribution-NonCommercial 3.0 Unported Licence.

32 L. Suresh and J. Y. Walz, *J. Colloid Interface Sci.*, 1996, **183**, 199–213.
33 L. Suresh and J. Y. Walz, *J. Colloid Interface Sci.*, 1997, **196**, 177–190.
34 C. Jin, T. Glawdel, C. L. Ren and M. B. Emelko, *Sci. Rep.*, 2015, **5**, 17747.
35 N. J. Wagner and J. F. Brady, *Phys. Today*, 2009, **62**, 27–32.
36 B. Schroyen, C.-P. Hsu, L. Isa, P. van Puyvelde and J. Vermant, *Phys. Rev. Lett.*, 2019, **122**, 218001.
37 B. Cichocki and R. B. Jones, *Phys. A*, 1998, **258**, 273–302.
38 G. C. Abade, B. Cichocki, M. L. Ekiel-Jeżewska, G. Nägele and E. Wajnryb, *J. Chem. Phys.*, 2012, **136**, 104902.
39 J. Riest, T. Eckert, W. Richtering and G. Naegele, *Soft Matter*, 2015, **11**, 2821–2843.
40 C. Kunert, J. Harting and O. I. Vinogradova, *Phys. Rev. Lett.*, 2010, **105**, 016001.
41 O. I. Vinogradova and A. V. Belyaev, *J. Phys. Condens. Matter*, 2011, **23**, 184104.
42 P. Ruckdeschel, M. Dulle, T. Honold, S. Förster, M. Karg and M. Retsch, *Nano Res.*, 2016, **9**, 1366–1376.
43 P. A. Midgley and M. Weyland, *Ultramicroscopy*, 2003, **96**, 413–431.
44 T. K. Moon, *IEEE Signal Process. Mag.*, 1996, **13**, 47–60.
45 A. J. Goldman, R. G. Cox and H. Brenner, *Chem. Eng. Sci.*, 1967, **22**, 637–651.
46 H. Brenner, *Chem. Eng. Sci.*, 1961, **16**, 242–251.
47 M. A. Bevan and D. C. Prieve, *J. Chem. Phys.*, 2000, **113**, 1228–1236.
48 H. C. Hamaker, *Physica*, 1937, **4**, 1058–1072.
49 S. Lin and M. R. Wiesner, *Langmuir*, 2010, **26**, 16638–16641.
50 J. S. Pedersen, *Adv. Colloid Interface Sci.*, 1997, **70**, 171–210.
51 H.-J. Wu and M. A. Bevan, *Langmuir*, 2005, **21**, 1244–1254.
52 H.-J. Wu, T. O. Pangburn, R. E. Beckham and M. A. Bevan, *Langmuir*, 2005, **21**, 9879–9888.
53 T. D. Iracki, D. J. Beltran-Villegas, S. L. Eichmann and M. A. Bevan, *Langmuir*, 2010, **26**, 18710–18717.
54 X. Shen, A. E. Wang, R. M. Sankaran and D. J. Lacks, *J. Electrost.*, 2016, **82**, 11–16.
55 S. H. Behrens and D. G. Grier, *J. Chem. Phys.*, 2001, **115**, 6716–6721.
56 B. Lennart, *Adv. Colloid Interface Sci.*, 1997, **70**, 125–169.
57 D. C. Prieve, *Adv. Colloid Interface Sci.*, 1999, **82**, 93–125.